Toward Real-Time Ground-Shaking-Intensity Forecasting Using ETAS and GMM: Insights from the Analysis of the 2022 Taitung Earthquake Sequence

Ming-Che Hsieh[*1], Chung-Han Chan[1,2], Kuo-Fong Ma[1,3], Yin-Tung Yen[4], Chun-Te Chen[4], Da-Yi Chen[5,6], and Yi-Wun Mika Liao[7,8]

Abstract

Earthquake forecasting, combined with precise ground-shaking estimations, plays a pivotal role in safeguarding public safety, fortifying infrastructure, and bolstering the preparedness of emergency services. This study introduces a comprehensive workflow that integrates the epidemic-type aftershock sequence (ETAS) model with a preselected ground-motion model (GMM), facilitating accurate short-term forecasting of ground-shaking intensity (GSI), which is crucial for effective earthquake warning. First, an analysis was conducted on an earthquake catalog spanning from 1994 to 2022 to optimize the ETAS parameters. The dataset used in this analysis allowed for the further calculation of total, background, and clustering seismicity rates, which are crucial for understanding spatiotemporal earthquake occurrence. Subsequently, short-term earthquake activity simulations were performed using these up-to-date seismicity rates to generate synthetic catalogs. The ground-shaking impact on the target sites from each synthetic catalog was assessed by determining the maximum intensity using a selected GMM. This simulation process was repeated to enhance the reliability of the forecasts. Through this process, a probability distribution was created, serving as a robust forecasting for GSI at sites. The performance of the forecasting model was validated through an example of the Taitung earthquake sequence in September 2022, showing its effectiveness in forecasting earthquake activity and site-specific GSI. The proposed forecasting model can quickly deliver short-term seismic hazard curves and warning messages, facilitating timely decision making.

Cite this article as Hsieh, M.-C., C.-H. Chan, K.-F. Ma, Y.-T. Yen, C.-T. Chen, D.-Y. Chen, and Y.-W. Mika Liao (2024). Toward Real-Time Ground-Shaking-Intensity Forecasting Using ETAS and GMM: Insights from the Analysis of the 2022 Taitung Earthquake Sequence, *Seismol. Res. Lett.* **XX**, 1–14, doi: 10.1785/0220240180.

Supplemental Material

Introduction

Earthquake protection is crucial for safeguarding both human lives and property. It is also indispensable for maintaining and operating critical infrastructures and factories for government and industry. Recently, earthquake early warning (EEW, e.g., Satriano *et al.*, 2011) is considered the most rapid response method in the face of an earthquake. All operations are immediately halted, with resumption contingent upon post-tremor conditions. However, EEW systems are unable to forecast the ground-shaking impacts that the public, governments, and industries may face within the next few hours or days, thus complicating the development of recovery strategies. For example, the 2016 Kumamoto earthquake in Japan featured a magnitude M_j 6.5 foreshock and a 7.3 mainshock, which occurred approximately one day apart, followed by aftershocks in the subsequent days (Kato *et al.*, 2016). The intense ground shaking rendered the disaster relief process challenging (Goda *et al.*, 2016). The rapid forecasting of earthquake occurrence in the days after a major earthquake, as well as the potential ground-shaking levels at specific sites, can influence the cascade of disaster relief and recovery strategies.

1. Earthquake Disaster and Risk Evaluation and Management Center (E-DREaM), National Central University, Taoyuan, Taiwan, https://orcid.org/0000-0002-5172-9016 (M-CH); https://orcid.org/0000-0003-1875-3652 (C-HC); https://orcid.org/0000-0002-4500-8079 (K-FM); 2. Department of Earth Sciences, National Central University, Taoyuan, Taiwan; 3. Institute of Earth Sciences, Academia Sinica, Taipei, Taiwan; 4. Disaster Prevention Technology Research Center, Sinotech Engineering Consultants (Inc.), Taipei, Taiwan, https://orcid.org/0000-0003-1338-3592 (Y-TY); https://orcid.org/0000-0003-3735-1317 (C-TC); 5. Seismological Center, Central Weather Administration, Taipei, Taiwan; 6. Department of Earth and Life, University of Taipei, Taipei, Taiwan; 7. GNS Science, Lower Hutt, New Zealand, https://orcid.org/0009-0000-1505-3496 (Y-WML); 8. School of Earth and Environment, University of Canterbury, Christchurch, New Zealand

*Corresponding author: mchsieh@ncu.edu.tw

In earthquake engineering, ground-motion models (GMMs) are commonly employed as a method for assessing the potential ground shaking that a site may experience (e.g., Lin and Lee, 2008; Wang, Lee, *et al.*, 2016). The GMM is used to estimate ground-motion parameters such as peak ground acceleration (PGA) and peak ground velocity (PGV) and to approximate ground-shaking intensity (GSI) at specific sites. However, although GMMs can rapidly provide ground-motion parameters, their effectiveness depends on accurate earthquake-source and site-specific parameters. Furthermore, GMMs are deterministic methods that do not incorporate concepts of probability and time. Therefore, GMMs must be combined with other probabilistic and time-dependent models to enable evaluations that consider the concept of temporal progression. For instance, the integration and application of the aforementioned models are revealed in probabilistic seismic hazard analysis (Cornell, 1968), enabling seismic hazard assessments on global (Pagani *et al.*, 2018, 2020) and national (Wang, Chan, *et al.*, 2016; Chan *et al.*, 2020) scales.

The epidemic-type aftershock sequence (ETAS, e.g., Ogata, 1988) model offers an alternative perspective by analyzing earthquake catalogs in conjunction with concepts including the Gutenberg–Richter (G-R) law (Gutenberg and Richter, 1944), the modified Omori–Utsu formula (Utsu, 1961; Utsu *et al.*, 1995), and spatial probability density functions (PDFs). This approach facilitates the characterization of seismicity within specific spatiotemporal ranges. Moreover, numerous studies have indicated that the ETAS model is suitable for short-term seismicity forecasting, highlighting its potential utility in capturing "the next earthquake" occurrence (e.g., Ogata, 2011, 2017; Ogata *et al.*, 2018). The ETAS model has been applied for time-dependent fault-rupture probability analysis, as described in the Uniform California Earthquake Rupture Forecast, Version 3 project (Field, Jordan, *et al.*, 2017; Field, Milner, *et al.*, 2017). Based on this approach, Zhuang (2011) examined the application of the space–time ETAS model for short-term earthquake forecasting in Japan. This framework presented online and offline tasks estimating ETAS parameters from recent seismicity and simulating earthquake occurrence. The framework demonstrated how to analyze earthquake catalogs with the ETAS model and conduct seismicity simulations, offering substantial efficacy for short-term earthquake occurrence forecasting. Similar studies have also shown that the ETAS model can forecast short-term earthquake occurrence. For example, Omi *et al.* (2013) introduced a real-time approach for forecasting aftershock rates using incomplete early observations, demonstrated through retrospective analysis of the 2011 Tohoku-Oki earthquake and further validated by recent seismic events in Japan; Omi *et al.* (2018) employed the ETAS model to devise an automatic aftershock forecasting system operational in Japan. Furthermore, the improved Bayesian-based ETAS model, using Markov chain Monte Carlo simulation, provides robust spatiotemporal seismicity forecasts, effectively demonstrated by the 2016 Amatrice earthquake sequence in Italy and the 2017–2019 Kermanshah earthquake sequence in Iran (Ebrahimian and Jalayer, 2017; Ebrahimian *et al.*, 2022).

This study builds on the work of Zhuang (2011), which provided an in-depth analysis of forecasting earthquake occurrences in real time. The approach described by Zhuang (2011) was chosen because of its validation through the Collaboratory for the Study of Earthquake Predictability project (e.g., Jordan, 2006; Zechar *et al.*, 2010). The 2D ETAS model is particularly suitable for quickly forecasting and simulating seismicity following moderate to large earthquakes in real time because of its computational efficiency. We have advanced the workflow by incorporating real-time seismicity rate calculation and conducting earthquake occurrence simulations in a high-performance computing environment. In addition, we integrate a ground-motion estimation module following the earthquake occurrence simulations. This module uses synthetic catalogs as inputs to the GMM to forecast site-specific GSI probability curves the next day every 30 min. A case study of the September 2022 Taitung earthquake sequence is presented to illustrate the workflow and forecasting results. This study demonstrates the contribution of our approach to short-term earthquake occurrence and the forecasting of site-specific GSI. This approach can be a valuable tool, as an extension of EEW, for short-term seismic hazard mitigation.

Seismotectonic Background and ETAS Analysis in Taiwan

Taiwan is located where the Philippine Sea plate and Eurasian plate interact, leading to subduction and collision processes. There are two subduction systems in the region, one involving the Philippine Sea plate to the north and the other involving the Eurasian plate to the east. The collision between the plates began in northern Taiwan during the late Miocene and has moved southward. Currently, central and southwestern Taiwan are experiencing the effects of this collision. In regions characterized by intricate seismotectonic structures and orogenic activity, earthquakes occur with high frequency. Consequently, conducting a statistical analysis of seismicity is crucial for seismic hazard assessment. Zhuang *et al.* (2005) used the ETAS model to separate background and clustering seismicity and analyzed the distribution of seismicity in relation to seismotectonic structures. Kawamura and Chen (2013) also used the ETAS model to identify precursory changes in seismicity before the 1999 Chi-Chi earthquake. Kawamura *et al.* (2014) applied statistical analysis, including the ETAS model, to analyze spatiotemporal changes in seismicity before and after the 2013 Nantou earthquake sequence.

Earthquake Catalog and Zonation

Estimating ETAS parameters requires careful selection of a spatiotemporal range that accurately represents seismicity characteristics because inaccuracies may result in nonconverging regression results or the inclusion of different geological units, leading to statistically insignificant outcomes. This study focuses on crustal earthquakes, with the "shallow regional source" zonations (depth ≤35 km) delineated by Cheng *et al.* (2015) being referenced. Earthquake location records within the coordinates of 119.8°–122.5° E and 21.7°–25.6° N were selected according to the zonation. In this study, a comprehensive retrieval of earthquake events from January 1973 to December 2022 was conducted using the Geophysical Database Management System (GDMS, Central Weather Administration, 2012; Shin *et al.*, 2013) as the input. This data were used to demonstrate real-time seismicity analysis with the ETAS model. The transition from trigger-based to continuous recording by the Central Weather Administration (CWA) in 1994 significantly enhanced the completeness of seismic waveform records and the accuracy of waveform and arrival-time identification in the earthquake catalog. Thus, this study analyzed earthquake location records from 1994 onward. The spatial distribution of earthquakes from 1994 to 2022 is shown in Figure 1. Cheng *et al.* (2015) specified that the magnitude of completeness (M_c) for Taiwan's earthquake catalog is ∼2.0–3.0. In this study, we used the maximum curvature method (e.g., Wiemer and Wyss, 2000) to analyze the magnitude of completeness of the CWA earthquake catalog from 1 January 1994 to 31 August 2022. The estimated *a*- and *b*-values are 7.05 and 0.84, respectively, with an M_c of 2.2, as shown in Figure 2a. The relationship between the event sequence numbers and magnitudes is plotted by closely examining the earthquake catalog from August to October 2022 and applying a dithering process to introduce random errors ranging from −0.05 to 0.05 to the earthquake magnitudes (Fig. 2b). This reveals that although the M_c can be set at 2.2 for August, there are gaps in the catalog before the 2022 Taitung earthquake sequence (labeled by 1). Following the foreshock and mainshock, significant gaps are observed in the catalog (labeled by 2–5), with M_c exceeding 3.0 during this period. From October onward, the M_c decreases to the range of 2.7–3.0 but remains higher than 2.2. Therefore, this result indicates that the issue of aftershock incompleteness, particularly in the short-term, affects the Taitung earthquake sequence, similar to the findings of Zhuang *et al.* (2017) for the Kumamoto, Japan, earthquake sequence. Based on the earthquake observation, we selected $M_c = 3.0$ as a conservative threshold to avoid inaccuracies in the ETAS model parameter estimation caused by potential data gaps during earthquakes.

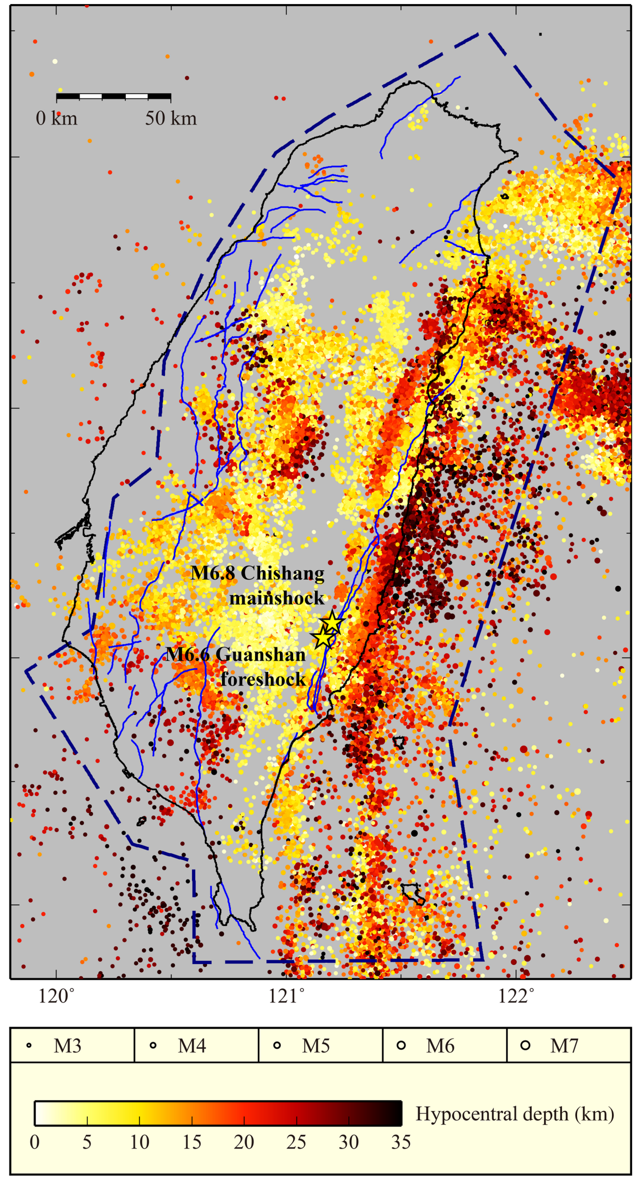

Figure 1. Earthquake distribution used in this study. The data depicted cover the period from 1994 to 2022, including earthquakes with magnitudes ≥3.0 and depths ≤35 km. In this figure, the circles' size and colormap represent the earthquakes' magnitude and depth, respectively. The navy dashed lines denote the union of the "shallow regional source" zonations by Cheng *et al.* (2015), and the blue lines indicate the inland fault distribution defined by Chan *et al.* (2020). The *M* 6.6 Guanshan foreshock and the *M* 6.8 Chishang mainshock of the 2022 Taitung earthquake sequence are shown in yellow stars. The color version of this figure is available only in the electronic edition.

Workflow Design

Overview

The workflow developed, referred to as the integrated online and offline approach of the Zhuang (2011), systematically engages in model parameter fitting for earthquake catalogs. It immediately acquires earthquake location records, simultaneously dispatched to online and offline systems. The offline component, which is computationally demanding, fits the ETAS parameters into the earthquake catalog. This task presents challenges for real-time forecasting because of its time-intensive nature. Conversely, the online system conducts real-time computations using prefitted ETAS parameters, thus circumventing immediate parameter fitting. This strategy optimally allocates computational

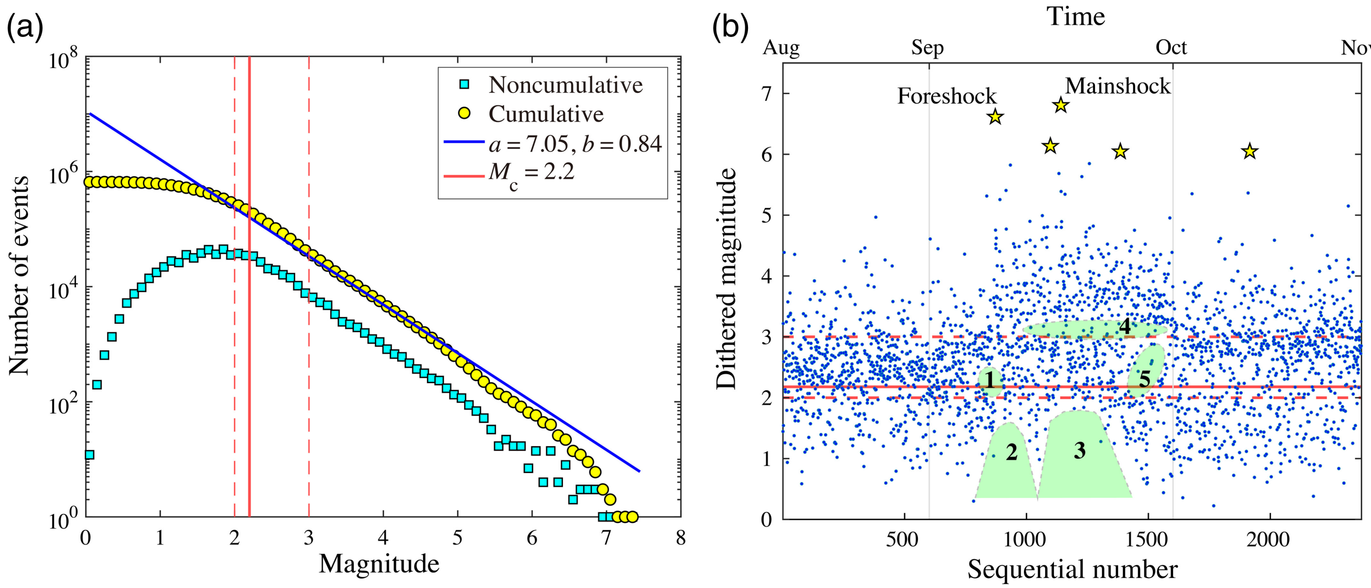

Figure 2. (a) Magnitude completeness analysis of the Central Weather Administration (CWA) earthquake catalog from 1 January 1994 to 31 August 2022, with a magnitude bin of 0.1. Cyan squares represent the number of earthquakes per magnitude interval and yellow circles represent the cumulative number of earthquakes. The blue line is the regression line ($a = 7.05$, $b = 0.84$). The red line marks $M_c = 2.2$, and the red dashed lines indicate M 2 and 3. (b) Earthquake events from August to October 2022 (blue dots). The lower horizontal axis shows events' sequential numbers, the upper axis shows months, and the vertical axis represents magnitudes after dithering. Earthquakes with magnitudes ≥6 are marked with yellow stars. Light green areas labeled 1–5 indicate potential gaps in the catalog. The solid and dashed red lines are the same as those shown in (a). The color version of this figure is available only in the electronic edition.

resources and facilitates the prompt estimation of seismicity rates. Upon completion of parameter fitting by the offline system, these parameters are transferred to the online system for updates, ensuring use of the most current data for forecasting purposes. In addition, the online system is tasked with the simulation of seismicity. Using the updated ETAS parameters, this simulation produces multiple short-term earthquake scenarios and generates synthetic catalogs. These catalogs facilitate the calculation of site-specific GSIs. With sufficient simulations, the system can determine the probability curves for exceeding specified GSIs at designated sites. Therefore, access to real-time earthquake location records enables the execution of seismicity rate calculations, short-term earthquake occurrence simulations, and forecasts of GSI probabilities through the online system. The workflow is illustrated in Figure 3, with the following sections providing detailed explanations of each component. In this study, 19 stations were selected as target sites for implementing real-time GSI forecasting (Fig. 4, Table 1). The CWA designated these 19 stations as representative seismic stations for each county and city.

Offline ETAS Model Parameter Estimation

We followed the expressions of the 2D ETAS model parameter estimation presented by Zhuang (2011). The earthquake catalog consolidates earthquake data, including their occurrence time, location, and magnitude. Through application of the ETAS model, the magnitude m is treated as an independent variable separate from other factors, and its distribution can be represented as

$$s(m) = \beta e^{-\beta(m-m_c)},\ m \geq m_c. \tag{1}$$

Equation (1) represents the PDF for earthquake magnitudes exceeding a certain threshold m_c, in which the parameter β is associated with the b-value from the G-R law, expressed as $\beta = b\ln(10)$. When analyzing an earthquake of magnitude m_i, the expected number of aftershocks it triggers within a specified spatiotemporal domain can be articulated through the conditional intensity function. This function is predicated upon the data observed prior to time t and the location (x_i, y_i) of the given event by

$$\lambda(t,x,y) = \mu(x,y) + \sum_{i:t_i<t} \xi(t,x,y;t_i,x_i,y_i,m_i). \tag{2}$$

$\lambda(t,x,y)$ denotes the total seismicity rate within a specific spatial range at the time t; $\mu(x,y)$ represents the background seismicity rate, which is assumed to be constant over time but varies by location; and $\xi(t,x,y,m;t_i,x_i,y_i,m_i)$ signifies the contribution to the seismicity rate from the ith event observed before the occurrence of time t. The units of λ, μ, and ξ are events/day/deg^2. Here, we denote ξ as the clustering seismicity rate, emphasizing the parent–offspring relationship between earthquake events. The clustering seismicity rate is

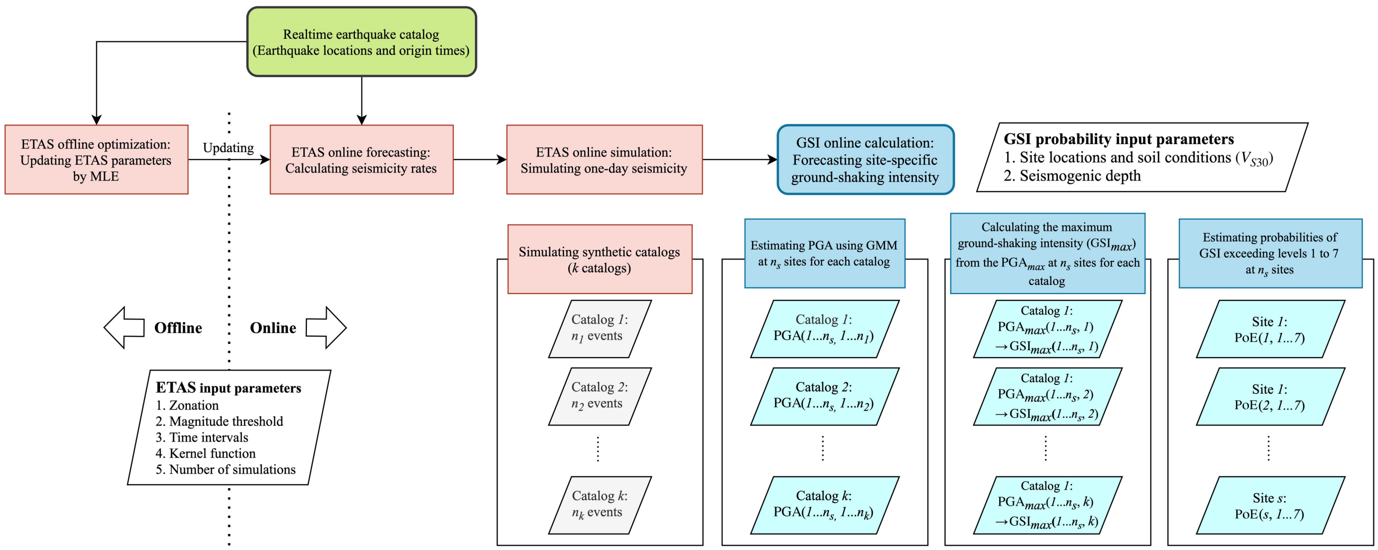

commonly assumed to be separable and contingent on significant variations in both time and spatial distances from the initiating event,

$$\xi(t,x,y;t_i,x_i,y_i,m_i) = k(m_i)g(t-t_i)f(x-x_i,y-y_i;m_i), \tag{3}$$

in which $k(m_i)$ (events) is the event productivity by an earthquake of magnitude m_i; $g(t-t_i))$ is the temporal PDF of the effective time lapse from an earthquake; and $f(x-x_i,y-y_i;m_i)$ is a spatial PDF, which describes the effective distance from an earthquake with the point-source assumption. Thus, these terms can be written as

$$k(m) = Ae^{\alpha(m-m_c)},\ m \geq m_c, \tag{4}$$

$$g(t) = \frac{p-1}{c}\left(1+\frac{t}{c}\right)^{-p},\ t > 0, \tag{5}$$

and

$$f(x,y;m) = \frac{q-1}{\pi De^{\gamma(m-m_c)}}\left[1+\frac{x^2+y^2}{De^{\gamma(m-m_c)}}\right]^{-q}. \tag{6}$$

In equations (4)–(6), A, α, c, p, D, q, and γ are undetermined parameters. If the background seismicity rate $\mu(x,y)$ is known, these model parameters can be iteratively estimated by the maximum-likelihood estimation (MLE) algorithm to maximize the likelihood function L from a spatial region S and a time interval $[0, T]$, and the model parameters are evaluated by Akaike information criterion (AIC, Akaike, 1974) to deal with the risk of overfitting or underfitting to the dataset:

$$\ln L = \sum_{i:(t_i,x_i,y_i)\in S\times[0,T]} \ln\lambda(t_i,x_i,y_i) - \int_0^T\iint_S \lambda(t,x,y)dxdydt + \sum_{i=1}^{N}\ln s(m_i). \tag{7}$$

Figure 3. Illustration of the workflow design of this study. The workflow is structured to include both online and offline components. The offline component is dedicated to estimating epidemic-type aftershock sequence (ETAS) model parameters, whereas the online component involves calculating seismicity rates, seismicity simulation, and the computation of ground-shaking intensity (GSI) probabilities. PGA, peak ground velocity; PoE, probability of exceedance. The color version of this figure is available only in the electronic edition.

According to the spatial range described in the Earthquake catalog and zonation section, the area is divided into 81 grid points along longitude and 201 along latitude. The seismicity rates are then calculated based on these grids. The background seismicity rate $\mu(x,y)$ can be estimated using the variable kernel estimation method (Zhuang *et al.*, 2002), which considers different searching bandwidths for smoothing seismicity through a Gaussian kernel function. This approach improves on the potential misestimation in seismic gap zones or areas of dense seismic activity when only a fixed bandwidth is selected. The procedure entails establishing a bandwidth threshold h_j for a Gaussian kernel function and computing based on the closest n_pth earthquakes. Commonly, h_j is ascertained to the earthquake location errors, with n_p typically ranging from 3 to 5. In this study, we referenced the earthquake catalog from the CWA, which posits a location error range of 2–3 km. Thus, we selected h_j as 3 km and fixed n_p at 5 to optimize the maximum-likelihood estimates. It is generally observed that conducting 3–7 iterations facilitates the achievement of stable and reliable convergence in the analysis.

Online Seismicity-Rate Calculation, Simulation, and GSI Probability Estimation

In practical forecasting operations, the online system primarily implements the following tasks: (1) calculating the total,

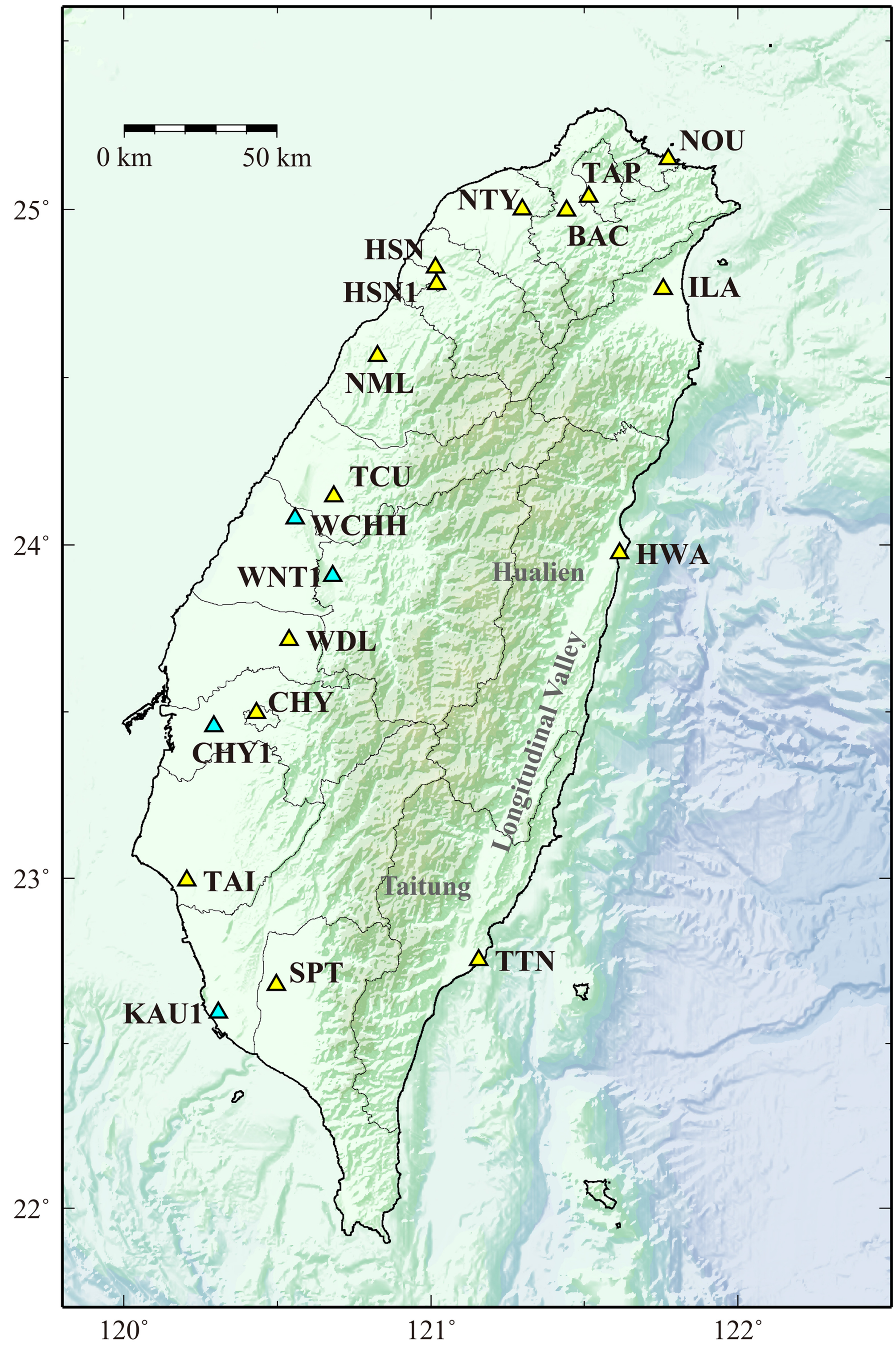

Figure 4. CWA seismic stations implemented in this study comprise 16 physical stations (yellow triangles) and 3 virtual stations (cyan triangles), each representing a county or city; solid lines within the island indicate administrative divisions. Taitung and Hualien counties and the Longitudinal Valley are also labeled on the map. See Table 1 for detailed station parameters. The color version of this figure is available only in the electronic edition.

background, and clustering seismicity rates; (2) using these rates to simulate one-day seismicity, thereby generating synthetic earthquake catalogs; (3) employing the selected GMM to calculate the PGA for each event in the catalog at specific sites and converting these values into GSIs; and (4) quantifying the frequency at each target site may experience specific intensity levels, normalized by the number of simulations, which is then converted into probabilities. After we have obtained the ETAS parameters from the regression described in the previous section, cumulative earthquake catalogs up to a certain time t can be used to estimate the total, background, and clustering seismicity rates using equation (2). Because earthquake location records continue to be added to the catalog, these rates are continually updated. Thus, at each time frame t, we adopt Algorithm B introduced by Zhuang (2011). This approach generates multiple sets of synthetic one-day earthquake catalogs by conducting seismicity simulations using ETAS parameters. In addition, Zhuang (2011) indicates that setting the number of simulations (k) to 10,000 ensures the stability of the results for simulating seismicity and deals with wrong estimations in areas of low-occurrence probabilities or near-model boundaries. The simulation outcomes are also smoothed using a kernel function to stabilize the results.

To estimate the ground motions at specific sites, it is necessary to preselect a GMM to predict site-specific ground shaking. Recently developed

TABLE 1
Information of Stations Used for Ground-Shaking Intensity (GSI) Forecasting

Station ID	Municipality or County	Collocated Strong-Motion Station ID	Longitude (°)	Latitude (°)	V_{S30} (m/s)	V_{S30} Reference	Note
TAP	Taipei City	TAP001	121.5138	25.0377	177.42	EGDT*	—
BAC	New Taipei City	TAP054	121.4418	24.9975	309.74	EGDT	—
NOU	Keelung City	TAP065	121.7731	25.1493	1034.66	EGDT	—
HSN1	Hsinchu City	TCU017	121.0182	24.7787	548.25	EGDT	—
NTY	Taoyuan City	TCU163	121.2977	24.9998	641.50	EGDT	—
HSN	Hsinchu County	TCU081	121.0142	24.8283	427.14	EGDT	—
ILA	Yilan County	ILA049	121.7563	24.7638	242.41	EGDT	—
TCU	Taichung City	TCU082	120.6842	24.1457	469.37	EGDT	—
NML	Miaoli County	TCU131	120.8257	24.5650	491.44	EGDT	—
WCHH	Changhua County	–	120.5583	24.0794	457.97	Lee and Tsai (2008)	Virtual station†
WNT1	Nantou County	–	120.6800	23.9070	500.10	Lee and Tsai (2008)	Virtual station
WDL	Yunlin County	CHY003	120.5385	23.7148	183.19	EGDT	—
KAU1	Kaohsiung City	–	120.3070	22.5940	189.65	Lee and Tsai (2008)	Virtual station
TAI	Tainan City	CHY085	120.2047	22.9933	272.65	EGDT	—
CHY	Chiayi City	CHY073	120.4325	23.4963	201.48	EGDT	—
CHY1	Chiayi County	–	120.2940	23.4570	228.79	Lee and Tsai (2008)	Virtual station
SPT	Pingtung County	KAU023	120.4960	22.6767	229.86	EGDT	—
HWA	Hualien County	HWA019	121.6135	23.9750	503.52	EGDT	—
TTN	Taitung County	TTN015	121.1548	22.7522	491.66	EGDT	—

*Engineering Geological Database for the Taiwan (EGDT) Strong-Motion Instrumentation Program (Kuo *et al.*, 2012; also see text in the Online Seismicity-Rate Calculation, Simulation, and GSI Probability Estimation section).
†CHY1, KAU1, WCHH, and WNT1 are designated as virtual stations for earthquake warning reports, using the ground-motion model for ground-shaking intensity estimation rather than serving as physical observation sites.

GMMs have demonstrated commendable performance (Chao *et al.*, 2020; Phung, Loh, Chao, and Abrahamson, 2020; Phung, Loh, Chao, *et al.*, 2020). However, the accompanying understanding of many physical properties and subsurface structures leads to a complex functional form. For example, considerations of engineering or seismological parameters, (e.g., the bedrock depths or the fault-rupture area) makes using the 2D and approximated point-source ETAS model less feasible. In this study, a GMM developed by Lin *et al.* (2011), referred to as LN11, was selected for analysis. The LN11 model was incorporated into the official seismic hazard map presented by the Taiwan Earthquake Model (Chan *et al.*, 2020). This model simplifies complexity by focusing on critical attributes, such as moment magnitude, rupture distance, hanging wall and footwall effects, and soil characteristics. The database for developing the GMM includes major earthquakes, thus making it an efficient and straightforward model for estimating ground shaking. While acknowledging that many current GMMs offer more precise ground-motion predictions, this study aims to demonstrate the feasibility of combining ETAS and GMM. Therefore, the relatively simple LN11 was chosen. Using the LN11 GMM allows for understanding the uncertainty distribution in ground-motion predictions, balancing feasibility to minimize sources of epistemic uncertainty. With the input of the aforementioned variables, it is possible to estimate the site-specific PGA. The former CWA GSI scale was adopted because of its exclusive consideration of PGA and simpler classification system, ranging from 1 to 7. In contrast, the updated scale incorporates PGV and expands the categorization to include levels such as five weak, five strong, six weak, and six strong (Central Weather Administration, 2019). The primary aim of this study is to demonstrate the feasibility of the entire GSI forecasting process. Thus, the simpler former scale is used as a reference for parameter conversion to reduce input parameters.

The V_{S30} site-condition term, representing the average shear-wave velocity in the top 30 m of a soil profile, is integrated

TABLE 2
Epidemic-Type Aftershock Sequence Parameters Obtained through Six Iterations of Maximum-Likelihood Estimation and the Akaike Information Criterion (AIC) Values for Each Iteration

*i*th Iteration	*A*	*c*	α	*p*	D^2	*q*	γ	–Ln *L*	AIC
1	0.8893	1.1651×10^{-3}	1.0747	1.0351	7.2347×10^{-4}	2.4019	0.3308	–54493.4	–108970.8
2	0.8984	1.1609×10^{-3}	1.0742	1.0347	7.2370×10^{-4}	2.4019	0.3307	–54494.4	–108972.8
3	0.9000	1.1602×10^{-3}	1.0741	1.0346	7.2377×10^{-4}	2.4020	0.3307	–54494.3	–108972.7
4	0.8999	1.1602×10^{-3}	1.0741	1.0346	7.2376×10^{-4}	2.4019	0.3307	–54494.3	–108972.7
5	0.8998	1.1602×10^{-3}	1.0741	1.0346	7.2376×10^{-4}	2.4019	0.3307	–54494.4	–108972.7
6	0.8999	1.1602×10^{-3}	1.0741	1.0346	7.2376×10^{-4}	2.4019	0.3307	–54494.4	–108972.7

into the functional forms of GMMs and significantly affects ground-motion estimation (Zhao and Xu, 2013; Kamai *et al.*, 2016). In this study, for a more accurate estimation of potential PGA at each site, V_{S30} values are sourced from the Engineering Geological Database for the Taiwan Strong Motion Instrumentation Program (EGDT, Kuo *et al.*, 2012). The EGDT database includes 489 site surveys associated with strong-motion stations, for which V_{S30} parameters are ascertained using both borehole logging data and standard penetration test evaluations. Some strong-motion stations in the EGDT database are collocated with the real-time stations, enabling direct access to the V_{S30} values for PGA estimations. For sites outside the coverage of the EGDT, V_{S30} parameters are interpolated using the comprehensive V_{S30} map of Taiwan (Lee and Tsai, 2008). This map, developed from 230 boring and *PS* logging data points at strong-motion stations, uses the geostatistical Kriging method for interpolation. Incorporating the V_{S30} parameter into the selected LN11 GMM used in this study was enabled.

The workflow leverages the 2D ETAS model to simulate earthquake occurrence, focusing solely on their spatiotemporal distribution and magnitude. However, these parameters, lacking simulated earthquake depth information, fall short of encompassing the essential variables required by the LN11 GMM for the GSI assessment. As a result, the allocation of depth distribution to these simulated earthquake events emerges as a critical analytical objective. In addressing this aspect, we refer to Wu *et al.* (2017), who depicted seismogenic depths from crustal earthquakes in Taiwan and discussed implications for seismic hazard assessment. The seismogenic depth from Wu *et al.* (2017) was adopted because their study considered the distributions of seismicity and earthquake moment release with depth. They defined seismogenic depth as the deep boundary encompassing 90% of crustal earthquakes in Taiwan, providing a representative and empirical depiction of potential depth variations for seismicity in the region. Our study incorporates the seismogenic depth distribution and assigns depths to simulated earthquakes through random value selection, extending from the surface to the maximum seismogenic depth. Even though 3D ETAS models (Guo *et al.*, 2015a; Guo *et al.*, 2018) provide a more detailed simulation of earthquake occurrences, they may require more computational time than 2D cases because of calculations on 3D grids. Consequently, our approach uses seismogenic depth distribution to reduce simulation time effectively, facilitating a more expedient methodology in the GSI forecasting model.

Using the preselected GMM and incorporating parameters of V_{S30} and seismogenic depth, the maximum PGAs at each site for every synthetic catalog can be calculated. These PGAs are then converted into GSIs according to the former CWA scale. Through the statistical analysis of 10,000 simulation results, the number of occurrences exceeding the specific shaking intensity level at each site can be determined. By dividing these counts by the total number of simulations (k), the probability of exceedance (PoE) of the specific shaking intensity at each site can be calculated.

To evaluate the computational efficiency of the workflow, the dataset comprising 59,471 earthquake location records was compiled by querying the GDMS. This dataset necessitated identifying parent–offspring relationships among the earthquakes, which was achieved by applying the stochastic declustering method. Based on the test dataset, ~96.5% used a 3 km bandwidth for the search range, but about 3.5% (2105 records) required an increase up to ~40 km. This validates the appropriateness of the zonation and depth range, indicating that most data points could be searched without significantly altering the kernel bandwidth, thus facilitating accurate probability estimation between events. Simultaneously, the ETAS parameters were regressed by six MLE iterations to ensure convergence (Table 2). The likelihood function and AIC values stabilize after the second iteration of six, indicating minimal changes in ETAS model parameters. Therefore, calculations were made for total, background, and clustering seismicity rates based on the interevent probability. The computations, executed on 96 central processing unit (CPU) cores from three Intel Xeon CPUs with a 2.6 GHz clock speed, were completed within approximately four hours. Access to pretrained parameters of the ETAS model allowed for using these optimized parameters to (1) perform stochastic

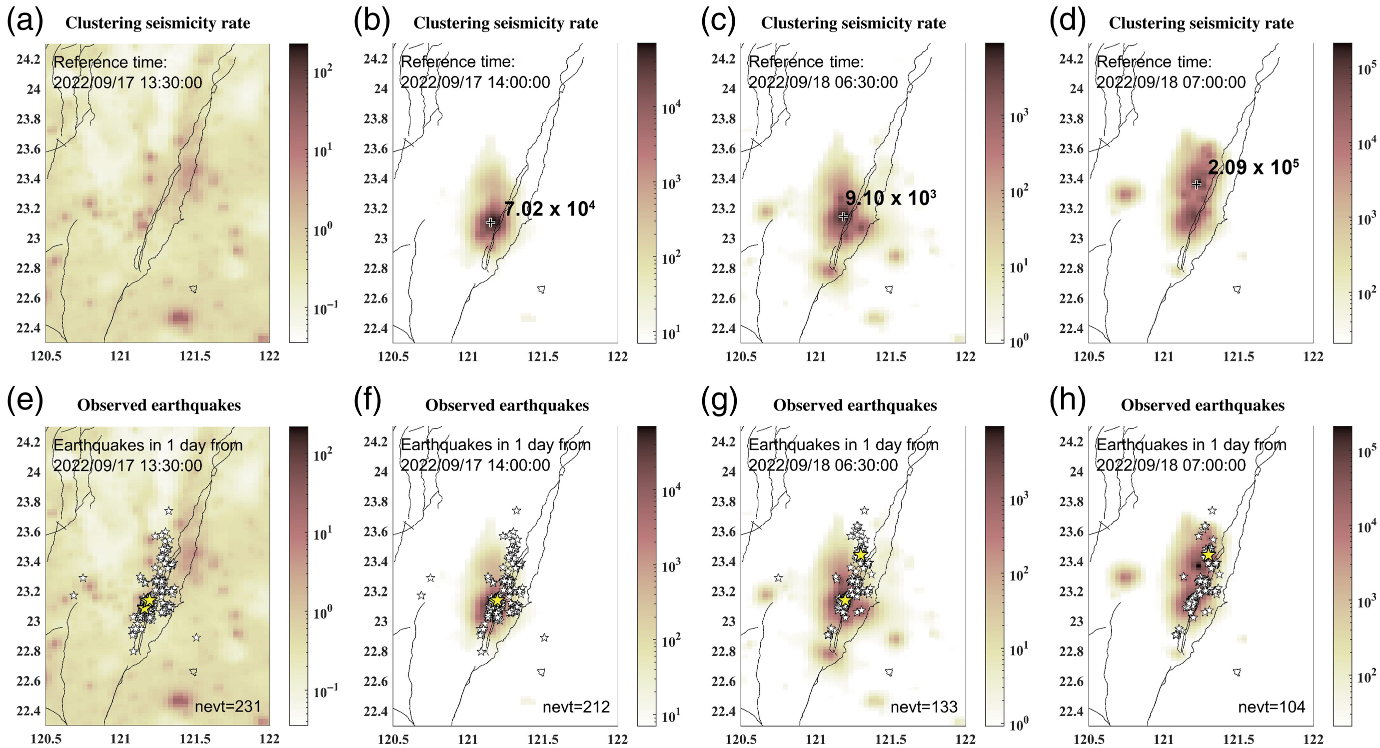

Figure 5. Changes in (a–d) clustering seismicity rates before and after the foreshock and the mainshock compared with (e–h) the distributions of one-day aftershocks. In each panel, the background color represents the clustering seismicity rate, with units indicated as events/day/ $\deg^2$. The calculation time is marked in the upper left corner of each panel. In panels (b–d), a plus sign marks the location of the maximum clustering seismicity rate. Earthquake events with a magnitude of ≥3.0 happening in one day of each recorded time are denoted by white stars in panels (e–h), and earthquakes with a magnitude of $M \geq 6$ are represented by yellow stars. The color version of this figure is available only in the electronic edition.

declustering and (2) compute seismicity rates, effectively reducing the required computational resources from 96 to 8 CPU cores. Under these conditions, the time required to calculate seismicity rates was significantly reduced to ~16 min. This marked reduction in computational demand supported the implementation of real-time earthquake occurrence forecasting. In addition, generating 10,000 one-day synthetic catalogs and conducting ground-motion estimation required only one CPU core, taking ~10 min. The overall process took about 26 min, enabling the conduction of site-specific GSI forecasts at 30-min intervals.

The 2022 Taitung Earthquake Sequence

On 17 September 2022, at 13:41 UTC, an M 6.6 earthquake took place in Guanshan, which was referred to as the foreshock, followed by an M 6.8 earthquake in Chishang on 18 September at 06:44 UTC, which was referred to as the mainshock (correspond locations of these events are shown in Fig. 1). The geological survey (Geological Survey and Mining Management Agency, 2022) inferred that the causative fault of the foreshock and the mainshock was a north-northeast-striking, west-dipping reverse fault with an angle of ~70° to 80°, resulting in surface ruptures. According to the search from the GDMS, the period from the foreshock occurrence to 25 September yielded 332 earthquake records with magnitudes >3. Most of these events were located in the Hualien and Taitung region, with their spatial distribution primarily on the western side of the southern section of the Longitudinal Valley (corresponding locations of Hualien and Taitung counties, and Longitudinal Valley are shown in Fig. 4), forming a narrow band. Temporally, earthquakes occurred from south to north, with numerous aftershocks concentrated between the foreshock and the mainshock. Lee *et al.* (2023) estimated the fault slip using finite-fault inversion techniques, revealing that most aftershocks occurred outside the assumed fault plane and in areas with high-slip patches.

Changes in Clustering Seismicity Rates before and after the Foreshock and Mainshock

The CWA catalog up to the end of 2022 was used to test 30-min interval forecasting of earthquake occurrences and site-specific GSI probability. Notable fluctuations in the clustering seismicity rate before and after the foreshock and mainshock were analyzed, particularly highlighting the relationship between seismicity rate changes and earthquake events (Fig. 5). Figure 5a shows a slight increase in seismic activity in Taitung 11 min before the foreshock, questioning its reliability as an indicator for an M_w 6.6 Guanshan earthquake. No apparent correlation was found between earthquake activity and seismicity rate

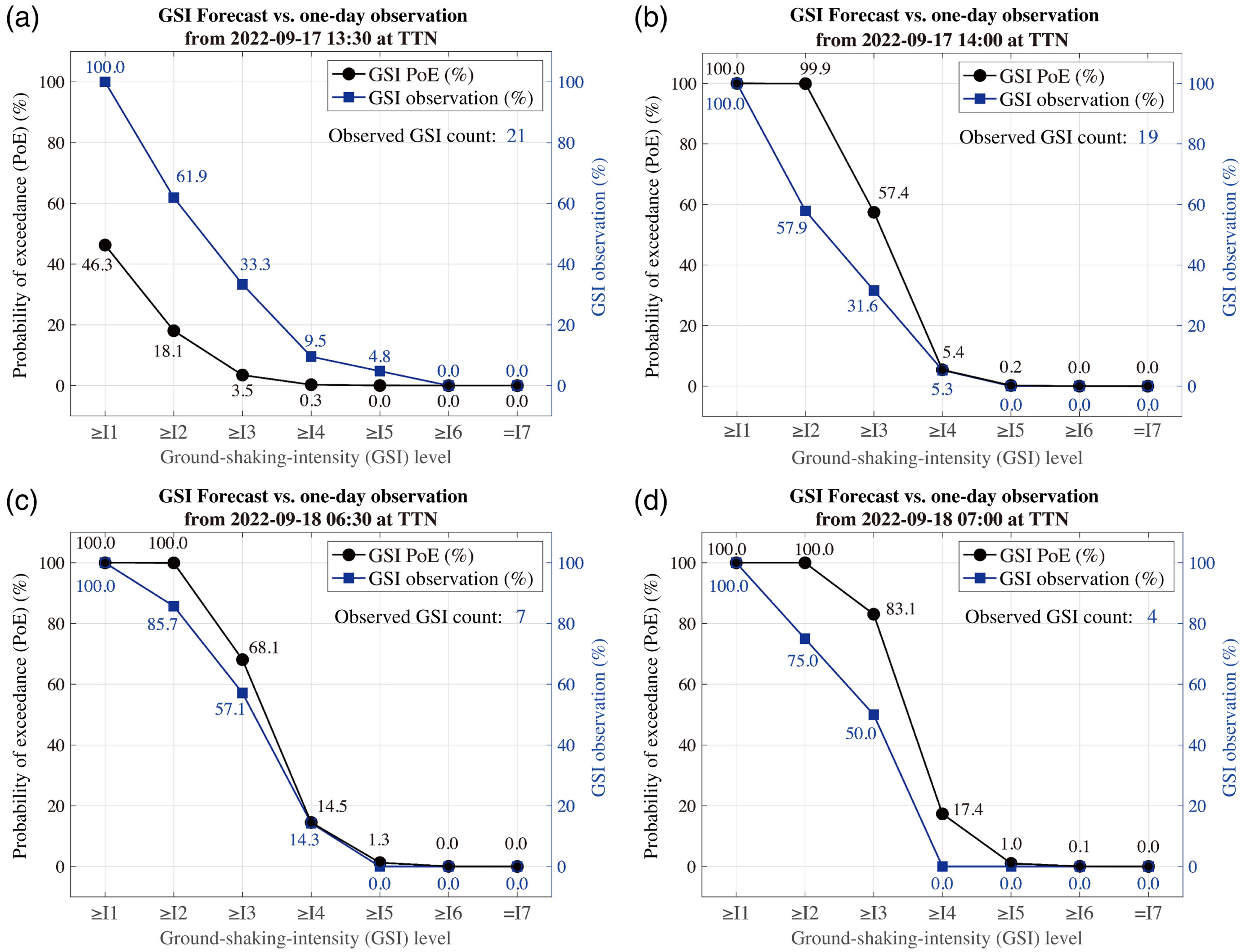

distribution the following day (Fig. 5b). However, a significant spike in the seismicity rate in Taitung was calculated 19 min after the foreshock (Fig. 5c), suggesting the foreshock's impact and the likelihood of imminent earthquakes. The 2D ETAS model, excluding fault geometry and earthquake depth, simplifies seismic sources as point sources, shown by a nearly concentric hotspot distribution. A comparison of seismicity rates with earthquake distribution one day after the foreshock reveals aftershocks clustered around the foreshock, extending northward (Fig. 5d). Prior to the mainshock, a decrease in the foreshock area's intensity was noted (Fig. 5e). Most aftershocks remained concentrated around the foreshock, with the impending mainshock positioned to the north (Fig. 5f). After the mainshock, seismicity rates increased significantly, influencing a long strip along the Longitudinal Valley (Fig. 5g), with aftershock distribution following this pattern the next day (Fig. 5h). These findings demonstrate that continuously updating earthquake data and integrating it into the 2D ETAS model significantly aid in analyzing moderate-magnitude earthquakes, estimating recent seismic activity, and understanding their spatiotemporal effects. From 17 to 24 September, changes in the clustering seismicity rate were recorded every 30 min, and comparisons were made with the seismicity within one day (Videos S1 and S2, available in the supplemental material to this article).

Figure 6. Changes in the GSI probability at the TTN station before and after the foreshock and the mainshock compared with the percentages of actual observed GSIs in one day: (a) before the foreshock, (b) after the foreshock, (c) before the mainshock, and (d) after the mainshock. In each panel, the black line represents the exceedance probability for GSI levels 1–7, and the blue line indicates the percentages of observations exceeding GSI level 1 (GSI-1). Note that the actual observed GSI count is denoted in the upper right corner of each panel. The color version of this figure is available only in the electronic edition.

Ground-Shaking-Intensity Probability Calculation

After 10,000 simulations at each calculation time, the GSI PoEs at 19 stations were calculated for periods before and after the foreshocks and mainshock and were compared with observed intensities. The TTN station, closest to the Taitung earthquake sequence area, was highlighted in Figure 6. Figure 6a shows that

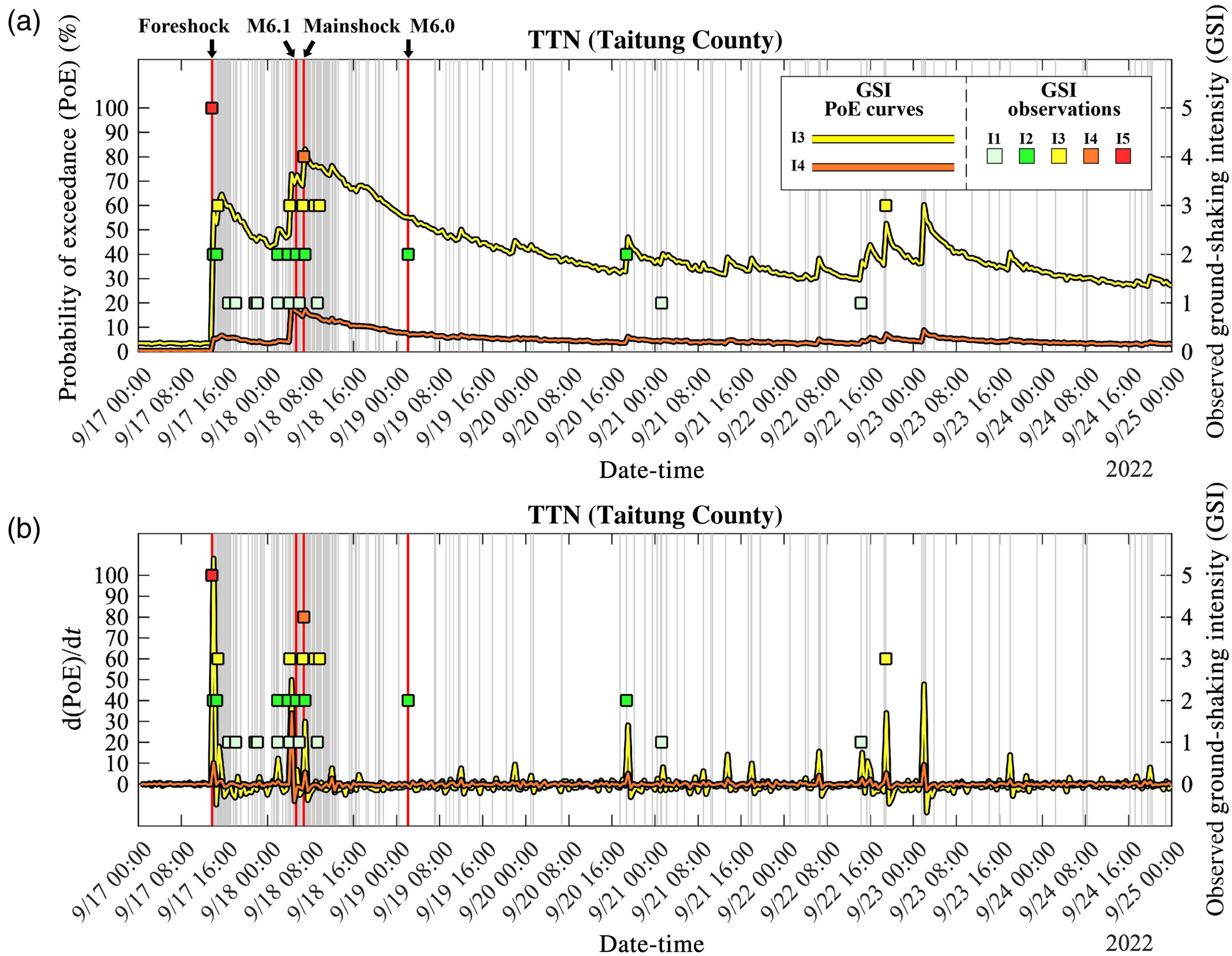

Figure 7. For the TTN station, (a) the forecast curves for GSI-3 and GSI-4 and (b) the first time derivatives of the GSI-3 and GSI-4 forecast curves, with (a) and (b) corresponding to the occurrence times of different GSIs, respectively. In (a) and (b), the vertical gray lines mark the occurrence times when $M \geq 3$ earthquakes took place in the study area, and the vertical red lines denote the occurrence times when $M \geq 6$ earthquakes happened. The color version of this figure is available only in the electronic edition.

before the foreshock, GSI PoEs were low across all levels. Although the trend was similar to observed intensities in one day, PoEs for higher intensities (e.g., GSI-3) were lower, showing limited awareness for severe events. Half an hour later, as Figure 5c indicates, a significant increase in seismicity rate was observed, leading to high-simulated frequencies of seismicity. Subsequent results indicated elevated GSI probabilities, with GSI-1 (0.8–2.5 gal) and GSI-2 (2.5–8 gal) nearing 100% and GSI-3 (8–25 gal) at 57.4%, a notable increase compared with earlier observations (Fig. 6b). This underscores the impact of real-time earthquake data on probability calculations. Before the mainshock, Figure 5e shows that a high-clustering seismicity rate continued in the foreshock area, maintaining high GSI probabilities at the TTN station. The persistent seismic activity kept GSI probabilities high (Fig. 6c). Finally, Figure 6d illustrates that after the mainshock, the seismicity rate significantly increased, boosting GSI probabilities, but observed GSI frequencies decreased. The results highlight that although time-specific calculations can forecast various GSI levels; the link between high probabilities and low-observed GSIs needs further exploration. The possible reason for high-GSI probabilities but low-GSI observation count right after the mainshock is that the mainshock occurred north of the TTN station, and the following aftershocks migrated northward with smaller magnitudes, resulting in fewer significant ground-shaking observations after the mainshock. Higher GSI probabilities were initially forecasted at the TTN station because of a higher clustering seismicity rate in the mainshock area. As time progressed, aftershocks and high-seismicity rate areas migrated northward, decreasing GSI probabilities at the TTN station over time.

To address this, PoE curves for GSI-3 and GSI-4 (25–80 gal) at the TTN station from 17 to 24 September were analyzed, as shown in Figure 7. Figure 7a demonstrates that the foreshock significantly impacted the GSI-3 and GSI-4 PoE curves, reaching a first peak. A second peak occurred after the mainshock, with GSI observations concentrated in the time interval between the foreshock and the M 6.0 aftershock, showing a strong correlation with the PoE curves. Although these findings suggest that high-GSI PoE occurrence time often aligns with observed GSIs, determining an appropriate threshold for alerts depends on user-specific earthquake protection needs. For example, whereas high-tech manufacturing might need alerts at lower probabilities because of sensitivity to vibrations, higher thresholds might be appropriate for general civil use. This study also explored the changes in these probabilities by taking the first derivative of the GSI-3 and GSI-4 PoE curves (Fig. 7b), revealing distinct spikes at the major peaks, which could serve as critical times for issuing GSI forecasts.

Discussion and Conclusions

This study introduces real-time earthquake occurrence and site-specific GSI forecasting using an ETAS model and a preselected GMM. Based on the workflow of Zhuang (2011), a ground-motion estimation module has been added that uses synthetic catalogs to produce site-specific GSI PoE curves, updated every 30 min for the following day. The workflow and forecasting capabilities are demonstrated through an example from the September 2022 Taitung earthquake sequence. This method can be integrated with regional or onsite EEW systems (Hsiao *et al.*, 2009, 2011; Wu, 2015).

For moderate- to large-magnitude earthquakes ($M \geq 6$), the ETAS model can also help with assessment. However, when considering fault dynamics, the complexity of the rupture process in moderate- to large-magnitude earthquakes means that factors related to the source, such as the selection of the rupture surface, rupture directivity, asperity distribution, rupture dimension, and regional stress disturbances and readjustments during the coseismic period, will impact the accuracy of earthquake occurrence forecasting. To overcome these limitations, Guo *et al.* (2015a, 2018) and Asayesh *et al.* (2023) introduced a 3D ETAS model that takes into account earthquake depth. In addition, Guo *et al.* (2015b, 2019) proposed an ETAS model considering fault-plane geometry. These models build on the existing 2D ETAS model to enhance the analysis of seismicity.

GSI forecasting is based on a relatively simple GMM for site-specific intensity estimation, which reduces the variability of different GMMs' impact on the GSI outcomes. Thus, the capacity to effectively handle the mapping uncertainty of ground-motion parameters is limited. If more suitable GMMs become available or additional physical parameters are integrated with the ETAS model, a better understanding and control over the uncertainty of ground-motion parameters could be achieved.

The PoE curves derived from this study are not just forecasts specific to particular sites but also hold a defined temporal relevance, serving as site-specific seismic hazard curves. In earthquake engineering, PoE curves for durations such as 30 or 50 yr are often used to evaluate the seismic hazard over a building's lifespan. However, the PoE curves developed in this research go beyond this, reflecting the impact of short-term seismic activity on specific sites. They serve as a reference for short-term seismic hazard analysis, offering valuable insights into the potential immediate risks at specific locations. This nuanced understanding of seismic hazards, tailored to each site's unique characteristics and needs, is a significant advancement. The temporal evolution of PoE curves emphasizes the importance of incorporating real-time data and continuous analysis into seismic hazard assessment strategies.

Data and Resources

The earthquake catalog used in this study were obtained from the Central Weather Administration (CWA), which are available to the public and can be downloaded from the Geophysical Database Management System (GDMS) of the CWA (https://gdms.cwa.gov.tw). The Generic Mapping Tools (GMT) is available at https://www.generic-mapping-tools.org. The codes for analyses were written by Fortran language, MATLAB (https://www.mathworks.com/products/matlab.html), Perl (https://www.perl.org), and R (https://www.r-project.org). All websites were last accessed in April 2024. The supplemental material for this article includes Videos S1 and S2, which show clustering seismicity rate changes every 30 min from 17 to 24 September and compare them with the earthquakes observed in one day.

Declaration of Competing Interests

The authors acknowledge that there are no conflicts of interest recorded.

Acknowledgments

The authors thank Editor-in-Chief Allison Bent, the guest editors, and two anonymous reviewers for their professional reviews and valuable suggestions. The authors thank Jiancang Zhuang for providing the epidemic-type aftershock sequence (ETAS) code used in this study and for constructive suggestions and comments. The authors thank the Central Weather Administration (CWA) for providing the data and the National Center for High-performance Computing (NCHC) for providing computational and storage resources. This work was supported through the National Science and Technology Council (NSTC) Grant Number 112-2116-M-008-016- and the CWA Grant Numbers MOTC-CWB-112-E-01 and MOTC-CWA-113-E-01. This work was also financially supported by the Earthquake Disaster & Risk Evaluation and Management Center (E-DREaM) from the Featured Areas Research Center Program within the framework of the Higher Education Sprout Project by the Ministry of Education (MOE) in Taiwan. The Taiwan Earthquake Research Center (TEC) Contribution Number for this article is 00191.

References

Akaike, H. (1974). A new look at the statistical model identification, *IEEE Trans. Automat. Contr.* **19,** no. 6, 716–723, doi: 10.1109/TAC.1974.1100705.

Asayesh, B. M., S. Hainzl, and G. Zöller (2023). Depth-dependent aftershock trigger potential revealed by 3D-ETAS modeling, *J. Geophys. Res.* **128,** no. 6, doi: 10.1029/2023jb026377.

Central Weather Administration (2012). Central Weather Administration seismographic network, doi: 10.7914/SN/T5.

Central Weather Administration (2019). Press release for modified seismic intensity scale, *Central Weather Administration*, available at https://www.cwa.gov.tw/Data/service/Newsbb/CH/1081218earthquakepress.pdf (last accessed April 2024) (in Chinese).

Chan, C. H., K. F. Ma, J. B. H. Shyu, Y. T. Lee, Y. J. Wang, J. C. Gao, Y. T. Yen, and R. J. Rau (2020). Probabilistic seismic hazard assessment for Taiwan: TEM PSHA2020, *Earthq. Spectra* **36,** no. 1, 137–159, doi: 10.1177/8755293020951587.

Chao, S. H., B. Chiou, C. C. Hsu, and P. S. Lin (2020). A horizontal ground-motion model for crustal and subduction earthquakes in Taiwan, *Earthq. Spectra* **36,** no. 2, 463–506, doi: 10.1177/8755293019891711.

Cheng, C.-T., P.-S. Hsieh, P.-S. Lin, Y.-T. Yen, and C.-H. Chan (2015). Probability seismic hazard mapping of Taiwan, in *Encyclopedia of Earthquake Engineering*, M. Beer, I. A. Kougioumtzoglou, E. Patelli, and S.-K. Au (Editors), Springer Berlin Heidelberg, Berlin, Heidelberg, 1–25.

Cornell, C. A. (1968). Engineering seismic risk analysis, *Bull. Seismol. Soc. Am.* **58,** no. 5, 1583–1606, doi: 10.1785/BSSA0580051583.

Ebrahimian, H., and F. Jalayer (2017). Robust seismicity forecasting based on Bayesian parameter estimation for epidemiological spatio-temporal aftershock clustering models, *Sci. Rep.* **7,** no. 1, 9803, doi: 10.1038/s41598-017-09962-z.

Ebrahimian, H., F. Jalayer, B. Maleki Asayesh, S. Hainzl, and H. Zafarani (2022). Improvements to seismicity forecasting based on a Bayesian spatio-temporal ETAS model, *Sci. Rep.* **12,** no. 1, 20,970, doi: 10.1038/s41598-022-24080-1.

Field, E. H., T. H. Jordan, M. T. Page, K. R. Milner, B. E. Shaw, T. E. Dawson, G. P. Biasi, T. Parsons, J. L. Hardebeck, A. J. Michael, *et al.* (2017). A synoptic view of the third uniform California earthquake rupture forecast (UCERF3), *Seismol. Res. Lett.* **88,** no. 5, 1259–1267, doi: 10.1785/0220170045.

Field, E. H., K. R. Milner, J. L. Hardebeck, M. T. Page, N. Van Der Elst, T. H. Jordan, A. J. Michael, B. E. Shaw, and M. J. Werner (2017). A spatiotemporal clustering model for the third uniform California earthquake rupture forecast (UCERF3-ETAS): Toward an operational earthquake forecast, *Bull. Seismol. Soc. Am.* **107,** no. 3, 1049–1081, doi: 10.1785/0120160173.

Geological Survey and Mining Management Agency (2022). 2022 Chihshang earthquake sequence geological survey report, *Geological Survey and Mining Management Agency, Ministry of Economic Affairs*, available at https://faultnew.moeacgs.gov.tw/Reports/More/63cc5a4b2020403d9f79d3c33a7aba0c (in Chinese).

Goda, K., G. Campbell, L. Hulme, B. Ismael, L. Ke, R. Marsh, P. Sammonds, E. So, Y. Okumura, N. Kishi, *et al.* (2016). The 2016 Kumamoto earthquakes: Cascading geological hazards and compounding risks, *Front. Built Environ.* **2,** doi: 10.3389/fbuil.2016.00019.

Guo, Y. C., J. C. Zhuang, and N. Hirata (2018). Modelling and forecasting three-dimensional-hypocentre seismicity in the Kanto region, *Geophys. J. Int.* **214,** no. 1, 520–530, doi: 10.1093/gji/ggy154.

Guo, Y. C., J. C. Zhuang, and Y. Ogata (2019). Modeling and forecasting aftershocks can be improved by incorporating rupture geometry in the ETAS model, *Geophys. Res. Lett.* **46,** no. 22, 12,881–12,889, doi: 10.1029/2019gl084775.

Guo, Y. C., J. C. Zhuang, and S. Y. Zhou (2015a). A hypocentral version of the space-time ETAS model, *Geophys. J. Int.* **203,** no. 1, 366–372, doi: 10.1093/gji/ggv319.

Guo, Y. C., J. C. Zhuang, and S. Y. Zhou (2015b). An improved space-time ETAS model for inverting the rupture geometry from seismicity triggering, *J. Geophys. Res.* **120,** no. 5, 3309–3323, doi: 10.1002/2015jb011979.

Gutenberg, B., and C. F. Richter (1944). Frequency of earthquakes in California, *Bull. Seismol. Soc. Am.* **34,** no. 4, 185–188, doi: 10.1785/BSSA0340040185.

Hsiao, N. C., Y. M. Wu, T. C. Shin, L. Zhao, and T. L. Teng (2009). Development of earthquake early warning system in Taiwan, *Geophys. Res. Lett.* **36,** no. 5, doi: 10.1029/2008gl036596.

Hsiao, N. C., Y. M. Wu, L. Zhao, D. Y. Chen, W. T. Huang, K. H. Kuo, T. C. Shin, and P. L. Leu (2011). A new prototype system for earthquake early warning in Taiwan, *Soil Dynam. Earthq. Eng.* **31,** no. 2, 201–208, doi: 10.1016/j.soildyn.2010.01.008.

Jordan, T. H. (2006). Earthquake predictability, brick by brick, *Seismol. Res. Lett.* **77,** no. 1, 3–6, doi: 10.1785/gssrl.77.1.3.

Kamai, R., N. A. Abrahamson, and W. J. Silva (2016). VS30 in the NGA GMPEs: Regional differences and suggested practice, *Earthq. Spectra* **32,** no. 4, 2083–2108, doi: 10.1193/072615EQS121M.

Kato, A., K. Nakamura, and Y. Hiyama (2016). The 2016 Kumamoto earthquake sequence, *Proc. Jpn. Acad. Ser. B* **92,** no. 8, 358–371, doi: 10.2183/pjab.92.359.

Kawamura, M., and C. C. Chen (2013). Precursory change in seismicity revealed by the Epidemic-Type Aftershock-Sequences model: A case study of the 1999 Chi-Chi, Taiwan earthquake, *Tectonophysics* **592,** 141–149, doi: 10.1016/j.tecto.2013.02.017.

Kawamura, M., C. C. Chen, and Y. M. Wu (2014). Seismicity change revealed by ETAS, PI, and Z-value methods: A case study of the 2013 Nantou, Taiwan earthquake, *Tectonophysics* **634,** 139–155, doi: 10.1016/j.tecto.2014.07.028.

Kuo, C.-H., K.-L. Wen, H.-H. Hsieh, C.-M. Lin, T.-M. Chang, and K.-W. Kuo (2012). Site classification and Vs30 estimation of free-field TSMIP stations using the logging data of EGDT, *Eng. Geol.* **129/130,** 68–75, doi: 10.1016/j.enggeo.2012.01.013.

Lee, C.-T., and B.-R. Tsai (2008). Mapping Vs30 in Taiwan, *Terr. Atmos. Ocean. Sci.* **19,** no. 6, doi: 10.3319/tao.2008.19.6.671(pt).

Lee, S. J., T. Y. Liu, and T. C. Lin (2023). The role of the west-dipping collision boundary fault in the Taiwan 2022 Chihshang earthquake sequence, *Sci. Rep.* **13,** no. 1, 3552, doi: 10.1038/s41598-023-30361-0.

Lin, P. S., and C. T. Lee (2008). Ground-motion attenuation relationships for subduction-zone earthquakes in northeastern Taiwan, *Bull. Seismol. Soc. Am.* **98,** no. 1, 220–240, doi: 10.1785/0120060002.

Lin, P.-S., C.-T. Lee, C.-T. Cheng, and C.-H. Sung (2011). Response spectral attenuation relations for shallow crustal earthquakes in Taiwan, *Eng. Geol.* **121,** nos. 3/4, 150–164, doi: 10.1016/j.enggeo.2011.04.019.

Ogata, Y. (1988). Statistical models for earthquake occurrences tand residual analysis for point processes, *J. Am. Stat. Assoc.* **83,** no. 401, 9–27.

Ogata, Y. (2011). Significant improvements of the space-time ETAS model for forecasting of accurate baseline seismicity, *Earth Planets Space* **63,** no. 3, 217–229, doi: 10.5047/eps.2010.09.001.

Ogata, Y. (2017). Forecasting of a large earthquake: An outlook of the research, *Seismol. Res. Lett.* **88,** no. 4, 1117–1126, doi: 10.1785/0220170006.

Ogata, Y., K. Katsura, H. Tsuruoka, and N. Hirata (2018). Exploring magnitude forecasting of the next earthquake, *Seismol. Res. Lett.* **89,** no. 4, 1298–1304, doi: 10.1785/0220180034.

Omi, T., Y. Ogata, Y. Hirata, and K. Aihara (2013). Forecasting large aftershocks within one day after the main shock, *Sci. Rep.* **3,** 2218, doi: 10.1038/srep02218.

Omi, T., Y. Ogata, K. Shiomi, B. Enescu, K. Sawazaki, and K. Aihara (2018). Implementation of a real-time system for automatic aftershock forecasting in Japan, *Seismol. Res. Lett.* **90,** no. 1, 242–250, doi: 10.1785/0220180213.

Pagani, M., J. Garcia-Pelaez, R. Gee, K. Johnson, V. Poggi, V. Silva, M. Simionato, R. Styron, D. Viganò, L. Danciu, *et al.* (2020). The 2018 version of the global earthquake model: Hazard component, *Earthq. Spectra* **36,** no. 1_suppl, 226–251, doi: 10.1177/8755293020931866.

Pagani, M., J. García-Pelaez, R. Gee, K. Johnson, V. Poggi, M. Simionato, R. Styron, D. Viganò, L. Danciu, D. Monelli, *et al.* (2018). GEM global seismic hazard map v.2018.1, doi: 10.13117/GEM-GLOBAL-SEISMIC-HAZARD-MAP-2018.1.

Phung, V. B., C. H. Loh, S. H. Chao, and N. A. Abrahamson (2020). Ground motion prediction equation for Taiwan subduction zone earthquakes, *Earthq. Spectra* **36,** no. 3, 1331–1358, doi: 10.1177/8755293020906829.

Phung, V. B., C. H. Loh, S. H. Chao, B. S. J. Chiou, and B. S. Huang (2020). Ground motion prediction equation for crustal earthquakes in Taiwan, *Earthq. Spectra* **36,** no. 4, 2129–2164, doi: 10.1177/8755293020919415.

Satriano, C., Y. M. Wu, A. Zollo, and H. Kanamori (2011). Earthquake early warning: Concepts, methods and physical grounds, *Soil Dynam. Earthq. Eng.* **31,** no. 2, 106–118, doi: 10.1016/j.soildyn.2010.07.007.

Shin, T.-C., C.-H. Chang, H.-C. Pu, H.-W. Lin, and P.-L. Leu (2013). The geophysical database management system in Taiwan, *Terr. Atmos. Ocean. Sci.* **24,** no. 1, 11, doi: 10.3319/TAO.2012.09.20.01(T).

Utsu, T. (1961). A statistical study on the occurrence of aftershocks, *Geophys. Mag.* **30,** 521–605.

Utsu, T., Y. Ogata, and R. S. Matsu'ura (1995). The centenary of the Omori Formula for a decay law of aftershock activity, *J. Phys. Earth* **43,** no. 1, 1–33, doi: 10.4294/jpe1952.43.1.

Wang, Y. J., C. H. Chan, Y. T. Lee, K. F. Ma, J. B. H. Shyu, R. J. Rau, and C. T. Cheng (2016). Probabilistic seismic hazard assessment for Taiwan, *Terr. Atmos. Ocean. Sci.* **27,** no. 3, 325–340, doi: 10.3319/Tao.2016.05.03.01(Tem).

Wang, Y. J., Y. T. Lee, K. F. Ma, and Y. C. Wu (2016). New attenuation relationship for peak ground and pseudo-spectral acceleration of normal-faulting earthquakes in offshore northeast Taiwan, *Terr. Atmos. Ocean. Sci.* **27,** no. 1, 43–58, doi: 10.3319/Tao.2015.08.17.01(T).

Wiemer, S., and M. Wyss (2000). Minimum magnitude of completeness in earthquake catalogs: Examples from Alaska, the Western United States, and Japan, *Bull. Seismol. Soc. Am.* **90,** no. 4, 859–869, doi: 10.1785/0119990114.

Wu, W. N., Y. T. Yen, Y. J. Hsu, Y. M. Wu, J. Y. Lin, and S. K. Hsu (2017). Spatial variation of seismogenic depths of crustal earthquakes in the Taiwan region: Implications for seismic hazard assessment, *Tectonophysics* **708,** 81–95, doi: 10.1016/j.tecto.2017.04.028.

Wu, Y.-M. (2015). Progress on development of an earthquake early warning system using low-cost sensors, *Pure Appl. Geophys.* **172,** no. 9, 2343–2351, doi: 10.1007/s00024-014-0933-5.

Zechar, J. D., D. Schorlemmer, M. Liukis, J. Yu, F. Euchner, P. J. Maechling, and T. H. Jordan (2010). The collaboratory for the study of earthquake predictability perspective on computational earthquake science, *Concurrency Comput. Pract. Ex.* **22,** no. 12, 1836–1847, doi: 10.1002/cpe.1519.

Zhao, J. X., and H. Xu (2013). A comparison of VS30 and site period as site-effect parameters in response spectral ground-motion prediction equations, *Bull. Seismol. Soc. Am.* **103,** no. 1, 1–18, doi: 10.1785/0120110251.

Zhuang, J., Y. Ogata, and D. Vere-Jones (2002). Stochastic declustering of space-time earthquake occurrences, *J. Am. Stat. Assoc.* **97,** no. 458, 369–380, doi: 10.1198/016214502760046925.

Zhuang, J. C. (2011). Next-day earthquake forecasts for the Japan region generated by the ETAS model, *Earth Planets Space* **63,** no. 3, 207–216, doi: 10.5047/eps.2010.12.010.

Zhuang, J. C., C. P. Chang, Y. Ogata, and Y. I. Chen (2005). A study on the background and clustering seismicity in the Taiwan region by using point process models, *J. Geophys. Res.* **110,** no. B5, doi: 10.1029/2004jb003157.

Zhuang, J. C., Y. Ogata, and T. Wang (2017). Data completeness of the Kumamoto earthquake sequence in the JMA catalog and its influence on the estimation of the ETAS parameters, *Earth Planets Space* **69,** no. 1, doi: 10.1186/s40623-017-0614-6.

Manuscript received 6 May 2024
Published online 26 July 2024